Report of the National Research Institute for Earth Science and Disaster Resilience, No. 84; January, 2020

Rupture Processes of the 2011 Tohoku-Oki Earthquake and Its Two *M*7-Class Aftershocks Derived Using Curved Fault Models

Wataru SUZUKI*, Shin AOI*, Haruko SEKIGUCHI**, and Takashi KUNUGI*

[*] *Network Center for Earthquake, Tsunami and Volcano,*
National Research Institute for Earth Science and Disaster Resilience, Japan
wsuzuki@bosai.go.jp, aoi@bosai.go.jp, kunugi@bosai.go.jp
[**] *Disaster Prevention Research Institute, Kyoto University, Japan*
sekiguchi.haruko.6u@kyoto-u.ac.jp

Abstract

The M_{JMA}9.0 Tohoku-Oki mega-thrust earthquake was followed by two large interplate earthquakes (M_{JMA}7.4 and 7.6) that occurred around the northern and southern ends of the mainshock source area within 30 min. We derived the rupture processes of the mainshock and the two *M*7-class aftershocks using the K-NET and KiK-net strong-motion waveform data. A curved fault model for each event was constructed from the geometry of the upper surface of the Pacific plate. The mainshock analysis revealed a complex rupture with a very large slip and a long duration in the shallow part, repeated rupture events in the deeper part, and slow southern rupture propagation. Meanwhile, the rupture processes of the two *M*7-class aftershocks were relatively simple in space and time. The slip areas of the mainshock, the two large aftershocks, the locations of the thrust-type earthquakes and the slow earthquakes (tectonic tremors and very-low-frequency earthquakes) were complementary. The northern one of the two large aftershocks occurred in the region where previous earthquakes with similar magnitudes had occurred, whereas the southern one was the largest earthquake in the region and no large earthquake had evidently ruptured its large slip area in the past approximately nine decades.

Key words: Source rupture process, Tohoku-Oki earthquake, Iwate-Oki earthquake, Ibaraki-Oki earthquake, Curved fault model, Strong-motion record

Introduction

The Tohoku-Oki mega-thrust earthquake of March 11, 2011, significantly impacted various fields of Japanese society. To understand the nature of this disastrous earthquake, many researches on the source rupture process have been performed using various geophysical datasets[1]. A general feature of the rupture process derived using the low-frequency strong-motion[2], teleseismic[3], GNSS[4], tsunami[5] waveforms, or crustal deformation data[6] is that there were large slips off Miyagi prefecture (Miyagi-Oki region) between the hypocenter's neighbor and the Japan Trench. The papers cited here are some examples and more results can be found in the aforementioned review[1]. The moment magnitude (M_W) derived by these studies varies between 9.0 and 9.1. In our previous paper[2),7)], we derived the rupture process from the strong-motion data assuming a rectangular fault model and discussed the relationship between the rupture model and the wave radiation process. The results showed that the Miyagi-Oki region, which had the largest slip in the shallow part, experienced a significant rupture event from the shallow part to the deeper part approximately 60 s after the initial break. This rupture of the whole area generated the notable phase found in the velocity waveforms at the southern Iwate, Miyagi, and northern Fukushima prefecture regions. Furthermore, in the Miyagi-Oki region, the shallower part generated a very low-frequency content (< 0.02 Hz) of the notable velocity phase, whereas the deeper slip largely contributed to the higher content in the analyzed frequency range (0.01–0.125 Hz). This indicates that the difference in the locations of the wave radiations depending on its frequency was found for the lower frequency range than that revealed

* Tennodai 3-1, Tsukuba, Ibaraki 305-0006, Japan

from the comparison of the slip distribution with the results of the backprojection analyses of higher frequency waveforms[8)], the source models for the broadband strong-motion simulation[9)], or the direct observation of the original acceleration[3)].

After the Tohoku-Oki event, the seismicity in and around its source area was highly increased. Among these earthquakes, two large thrust aftershocks having magnitudes greater than 7.0 occurred in the northern and southern parts of the Tohoku-Oki source area within 30 min of the mainshock (**Fig. 1**). The northern aftershock took place off Iwate prefecture (Iwate-Oki region) at 15:08 (JST=UTC+9), 22 min after the mainshock. The Japan Meteorological Agency (JMA) reported its magnitude (M_{JMA}) to be 7.4 and M_{W} determined by the National Research Institute for Earth Science and Disaster Resilience (NIED) using the regional broadband seismograph network named F-net[10)] was also 7.4. At 15:15, the southern aftershock occurred off Ibaraki prefecture (Ibaraki-Oki region), with M_{JMA} of 7.6 and F-net M_{W} of 7.8. This event was the largest aftershock of the Tohoku-Oki earthquake. There had been no earthquakes with a registered M_{JMA} of larger than 7.2 off the Pacific coast of the Tohoku and Kanto regions since the M_{JMA}7.6 Sanriku-Haruka-Oki earthquake in 1994. These two aftershocks are significant considering the source characteristics and strong-motion generation of subduction-zone interplate earthquakes. Particularly, the southern one, i.e., the Ibaraki-Oki event, brought large shakings to the Kanto region, and also caused severe liquefaction together with the mainshock[11)]. However, the characteristics of these aftershocks were not sufficiently examined, hidden by the great impact of the Tohoku-Oki mainshock. Therefore, it is important to capture the rupture behaviors of these large aftershocks as well as the mainshock by taking a consistent analysis procedure for each earthquake.

The source area of these earthquakes extended such a vast area of approximately 500 km × 200 km that the strike and dip angles changed not so drastically but surely over the whole area of the Tohoku-Oki earthquake sequence. Therefore, it is desirable to derive the rupture models using curved faults that fully consider the plate geometry for examination of the spatial relationship among the earthquakes or further ground motion simulation using realistic three-dimensional underground structure models. In this study, we inferred the rupture processes of the 2011 Tohoku-Oki earthquake and its two M7-class aftershocks on the same plate interface model and examined the relationship among the earthquake sequence. K-NET and KiK-net by NIED, strong-motion networks deployed all over Japan[12),13)], recorded plenty of good-quality strong-motion waveforms for these three earthquakes. The waveforms of the two aftershocks could be influenced by the mainshock seismic waves. For example, a

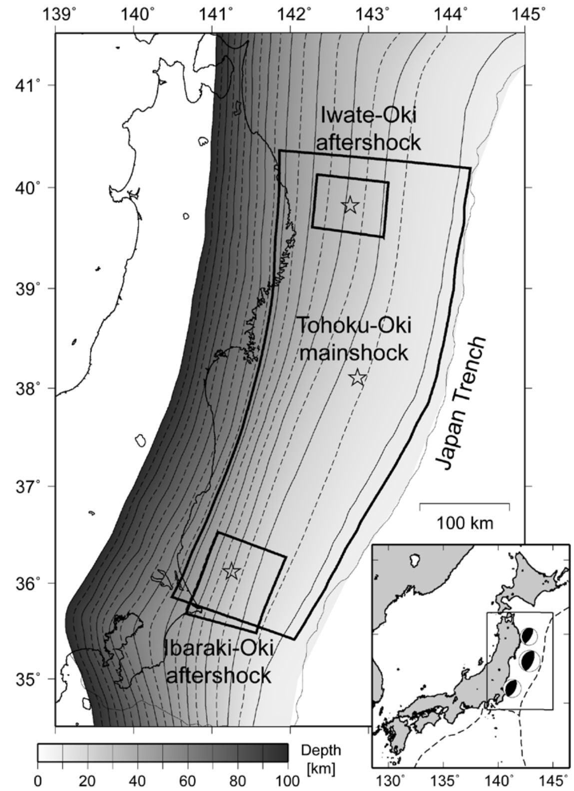

Fig. 1 Geometry of the upper surface of the Pacific plate (thin and dashed contours) and fault models used for the source inversion analysis (bold polygons). The thin solid contour lines denote the depths from 10 km to 100 km by 10 km and the dashed ones denote the depths from 15 km to 95 km by 10 km.

centroid moment tensor (CMT) analysis using the teleseismic data had difficulty in analyzing early aftershocks and could not determine the solution of the Iwate-Oki aftershock due to "the mainshock's strong excitation of long-period, slowly attenuating overtone modes" [14)]. Meanwhile, as such a very low-frequency content was less dominant in the regional strong-motion waveforms, the strong-motion dataset from K-NET and KiK-net can provide the valuable information on the spatio-temporal rupture behavior of the two aftershocks as well as the mainshock. We therefore used these strong-motion data for the source inversion analysis in this study.

2. Source Inversion Analysis Using a Curved Fault Model

The three earthquakes to be analyzed occurred between the subducting Pacific plate and the overriding continental plate. The geometry of the upper surface of the Pacific plate used in this study (**Fig. 1**) was based on the Japan Integrated Velocity Structure Model (JIVSM)[15)], which was constructed from a compilation of the geological and geophysical exploration data, and modification with the observed seismic waveforms and spectra, following a standardized procedure[16)]. The

Table 1 Hypocenter information and fault models of the three earthquakes analyzed in this study. (*Information by the JMA)

	Mainshock	Iwate-Oki	Ibaraki-Oki
Origin time (JST)*	14:46:18	15:08:53	15:15:34
Epicenter*	38.1035°N, 142.8610°E	39.8207°N, 142.7668°E	36.1208°N, 141.2525°E
Magnitude*	9.0	7.4	7.6
Depth of the Pacific plate at epicenter	16.4 km	28.7 km	29.9 km
Horizontal interval of subfault	20 km	6 km	10 km
Depth interval of subfault with depth range in parenthesis	1.6 km (8.8–12 km) 2.65 km (12–14.65 km) 3.5 km (14.65–18.15 km) 4.15 km (18.15–22.3 km) 5.2 km (22.3–27.5 km) 7 km (27.5–34.5 km) 9.1 km (34.4–52.7 km)	1.5 km (18.95–32.45 km) 1.55 km (32.45–35.55 km) 1.6 km (35.55–38.75 km)	2 km (15.5–21.55 km) 2.5 km (21.55–24.05 km) 3.5 km (24.05–31.05 km) 4 km (31.05–43.05 km)

geometry of the Pacific plate at shallower depths was constrained mainly by the geophysical exploration results.

The original JIVSM dataset describes the plate geometry by the depths at each horizontal grid. To flexibly construct fault models of the three interplate earthquakes from the plate model, we first made depth contours, and then selected representative points on the surface whose latitudes were within 35°N and 40.5°N. The representative points were selected so that their horizontal locations corresponded to the points at which the straight lines representing the plate-dipping directions at the regions intersected the contours of representative depths. The number of the straight lines was 56 and the representative depths ranged from 8 km to 80 km basically in increments of 2 km, except for shallow regions where the dip angle is very low. The representative point set also included the points on the plate surface at the JMA epicentral location of the three analyzed earthquakes (**Table 1**). As a result, the numbers of the representative depths and representative points were 38 and 2,128. After this, a curved surface that passes through the representative points was generated using the non-uniform B-spline[17]. Using the two parameters u and v ($0 \leq u, v \leq 1$), any point on the surface can be described as equation (1).

$$\begin{aligned} \boldsymbol{P}(u,v) &= \left(x(u,v), y(u,v), z(u,v)\right) \\ &= \sum_{i=0}^{n_u-1} \sum_{j=0}^{n_v-1} N_{i,m_u}(u) N_{j,m_v}(v) \boldsymbol{q}_{ij} \end{aligned} \quad (1)$$

Here, $N_{,m}$ denotes a B-spline basis function of m degrees, and $\boldsymbol{q}$ denotes a control point. Subscripts i and j are the indexes for the u and v directions. Note that the control points are different from the representative points extracted to generate the curved surface. They are usually located outside of the surface and can be derived by solving simultaneous equations made from representative points and end point condition. In this study, we used third-degree B-spline functions (m=3). The u direction was assigned to the horizontal direction on the fault, i.e., along-strike direction, and the v direction was assigned to the vertical downward direction. Therefore, the constant v corresponds to the iso-depth contour. An advantage of using equation (1) is that we can strictly generate local geometry at any point on the fault. The strike angle is derived as an angle between a vector $\boldsymbol{s}$ calculated from equation (2) and a horizontal axis to the north.

$$\boldsymbol{s} = \partial \boldsymbol{P} / \partial u \quad (2)$$

The dip angle is derived as an angle between the normal vector $\boldsymbol{n}$ calculated from equation (3) and a vertical axis.

$$\boldsymbol{n} = (\partial \boldsymbol{P}/\partial u \times \partial \boldsymbol{P}/\partial v) / \|\partial \boldsymbol{P}/\partial u \times \partial \boldsymbol{P}/\partial v\| \quad (3)$$

Area S can be calculated using equation (4).

$$S = \int \|\partial \boldsymbol{P}/\partial u \times \partial \boldsymbol{P}/\partial v\| du dv \quad (4)$$

We employed the multi-time-window linear waveform inversion scheme[18),19)]. In this inversion scheme, a rupture process is discretized spatially into subfaults and temporally into time windows at the subfaults. Thus, the spatio-temporal seismic moment on the fault is linearly related to the strong-motion waveforms via Green's functions according to the representation theorem. We assumed that each subfault comprised 25 point sources at which the Green's function was calculated, by aligning five point sources on each of the five depth contours, for consideration of the rupture propagation effect inside the subfaults[20)]. To construct fault models for the inversion analysis from the plate model represented by the non-uniform B-spline, we generated the

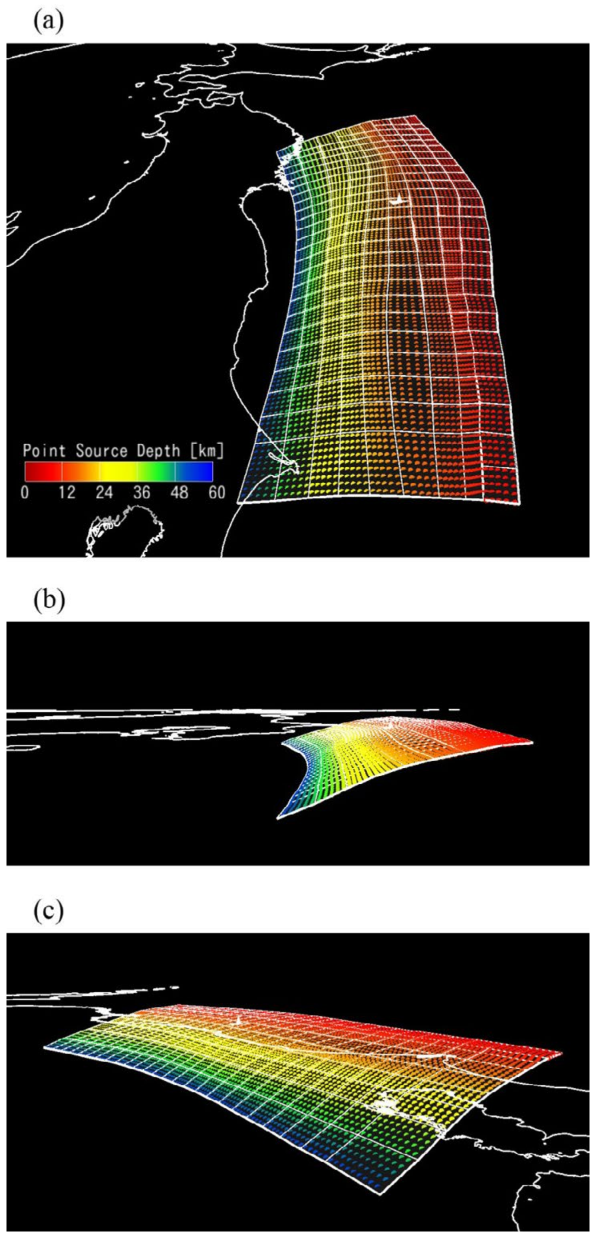

Fig. 2 Overhead view of the curved fault model constructed for the mainshock inversion analysis observed from (a) south with high depression angle, (b) south with low depression angle, and (c) southwest. The circles denote point sources colored according to the depths and the white lines denote the boundaries of the subfaults.

point sources at a prescribed uniform horizontal interval for each iso-depth contour sampled at prescribed depths. This was done by sequentially searching parameter u that reproduces the point separated by the prescribed distance from the neighboring point with fixed v in equation (1). The generation of point sources started from the representative point located at the JMA epicenter, which was assumed as the rupture starting point. Subfaults were then generated by grouping these point sources. In this procedure, the same horizontal length or along-strike length of the subfault could be set over the entire fault model. Meanwhile, the subfault width or along-dip length could not be constant as the dip angle varies along the iso-depth contours. The overhead view of the constructed fault model for the mainshock is shown in **Fig. 2**. The subfaults at the northern and southern ends have more point sources than 5 × 5 to fill the assumed fault area with equally-spaced points along the strike direction. **Table 1** shows the information of the fault models of the three analyzed earthquakes.

We used an isosceles triangle as a time window or temporal basis of inversion analysis, which was convolved with the Green's function as the source time function. A first time window at each point source was set at a time prescribed by a sphere expanding from the rupture starting point with a constant velocity (Vr). The following successive time windows were aligned at an interval of a half of the time-window duration. The Green's functions were calculated using the discrete wavenumber method[21] and the reflection and transmission matrix method[22] on the assumption of a one-dimensional underground structure model. The structure model was the same as that used in our previous papers[2),7)], which was constructed for each observation station.

The kinematic source rupture process was derived by solving equation (5) for the spatio-temporal moment rate, $\boldsymbol{m}$.

$$\begin{pmatrix} G \\ \lambda S \end{pmatrix} \boldsymbol{m} = \begin{pmatrix} \boldsymbol{d} \\ 0 \end{pmatrix} \qquad (5)$$

G is a matrix comprising Green's function corresponding to each time window of each subfault, and $\boldsymbol{d}$ denotes the data vector. The inversion data in this study was the S-wave portion of the strong-motion velocity waveforms, normalized by the maximum amplitude of three-component data for each station. The non-negative least squares method[23] was used to stabilize the inversion by limiting a slip angle variation. A reference slip angle at each subfault was obtained by projecting the slip direction indicated by the moment tensor solution onto the plane spanned by the strike and dip angles at the point. We produced the other stabilizing constraint by adding matrix S that makes the slip amount and direction vary smoothly in space and time[24]. The smoothing strength λ has sometimes been determined by Bayesian approach[24),25)]; however, this approach often results in a weaker strength than expected[26]. Therefore, we chose the smoothing strength that provided a reasonable result regarding waveform fitting, roughness of the slip distribution, and seismic moment.

3. M_{JMA}9.0 Tohoku-Oki Mainshock

3.1 Data and Analysis

We used the same strong-motion dataset as our previous study using the rectangular fault model[2),7)]. The dataset comprises the three-component velocity waveforms bandpass-filtered between 0.01 and 0.125 Hz at the 10 K-NET surface stations and 26 KiK-net borehole stations (**Fig. 3**). The records for the inversion started 10 s before the *S*-wave arrival time. Their durations varied among the stations depending on the length of triggered data and the amplitudes of the later phases.

The construction procedure of the curved fault model of the mainshock and its geometry were described in the previous section and in **Fig. 2**. The subfaults were intended to have a horizontal length of 20 km and an along-dip width greater than 20 km (**Table 1**). Near the northern and southern ends of the fault, the horizontal length tends to be greater than 20 km. In addition, the along-dip width around these ends may be smaller than 20 km due to a steeper dip angle than that in the central area of the fault.

Our previous papers[2),7)] presented a distinguishing rupture pattern of the Tohoku-Oki event in the Miyagi-Oki region, where the slip continued for a very long duration in the shallow part, and the two rupture events occurred around the hypocenter and down to deeper part. To fully describe such a complex rupture process, it is necessary for time windows to cover a sufficiently long, possible slip duration. However, allowing a long slip duration over an entire fault possibly results in over-parameterization and produces unrealistic slips. Therefore, we first performed an inversion allowing 93-s slip duration after the first time window starting time prescribed by *Vr* for the whole fault area, by assigning 30 time windows, each of which had a 6-s duration separated by 3 s. In this preliminary analysis, the inversion with *Vr* = 3.2 km/s provided the smallest residual value among the inversions with *Vr* ranging from 2.0 km/s to 4.0 km/s in increments of 0.4 km/s. The inversion result indicates that it is desirable to assume a longer slip duration for subfaults around the rupture starting point, whereas that for the subfaults in the northern and southern parts can be reduced. In addition, the slip of the southern subfaults started much later than the first time window starting time described by *Vr*, suggesting slower rupture propagation.

Considering these rupture characteristics found in the preliminary analysis, we performed the inversion using the different number of time windows and a variable velocity *Vr* depending on the location of the subfaults. **Fig. 3** shows the first time window starting time and an allowed maximum duration for each subfault. *Vr* was 3.2 km/s for the subfaults whose latitudes are greater than 37.9°N. For the southern subfaults, the first time window starting time was calculated using *Vr* of 3.2 km/s up to 70 km from the rupture starting point and a slower *Vr* of 2.3 km/s beyond 70 km. We allowed a 108-s slip duration for the subfault of the rupture starting point because the longer slip duration had been required for

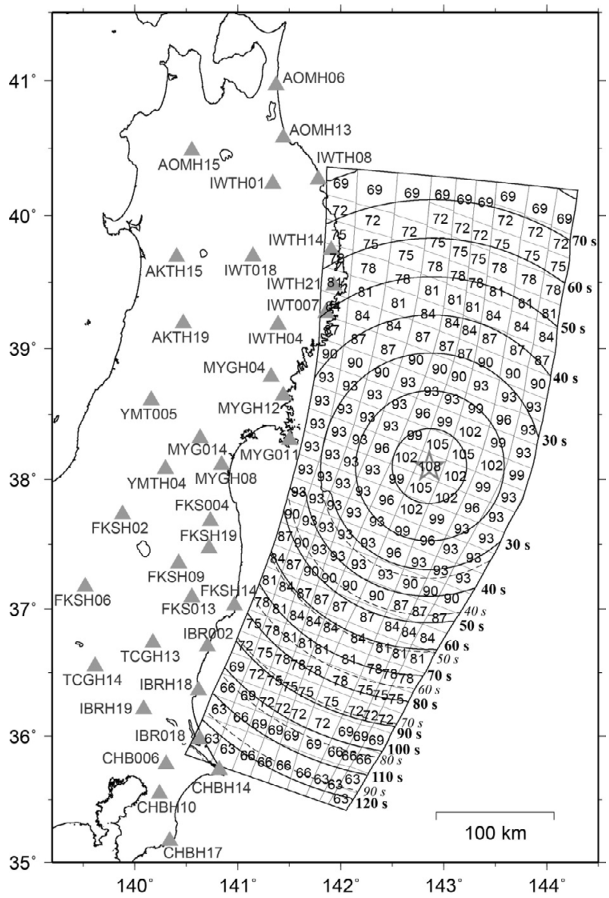

Fig. 3 Strong-motion stations (triangles), first time window starting time (solid contours on fault model with bold numerals), and allowed maximum slip duration in seconds (numerals on fault model) used for the mainshock inversion analysis. A star denotes the rupture starting subfault. The dashed contours with italic numerals are the first time window starting times calculated from *Vr* of 3.2 km/s over the entire fault.

subfaults around the rupture starting point in the preliminary analysis. The allowed slip duration or the number of time windows was decreased with the distance from the rupture starting subfault. Then, it was shorter than 70 s at the subfaults in the northern and southern ends.

3.2 Result

Fig. 4 shows the derived mainshock rupture model, in terms of (a) the total slip distribution, (b) the rupture progression process, and (c) the slip velocity time function of each subfault. From the panel of the total slip (**Fig. 4a**), large slips were observed for the Miyagi-Oki region, where the hypocenter was located. The shallower part of the region had a larger slip, which reached the maximum slip of 59 m. A relatively large slip of 10 m was estimated off Fukushima prefecture (Fukushima-Oki region) at depths deeper than the rupture starting point. The total seismic moment of this

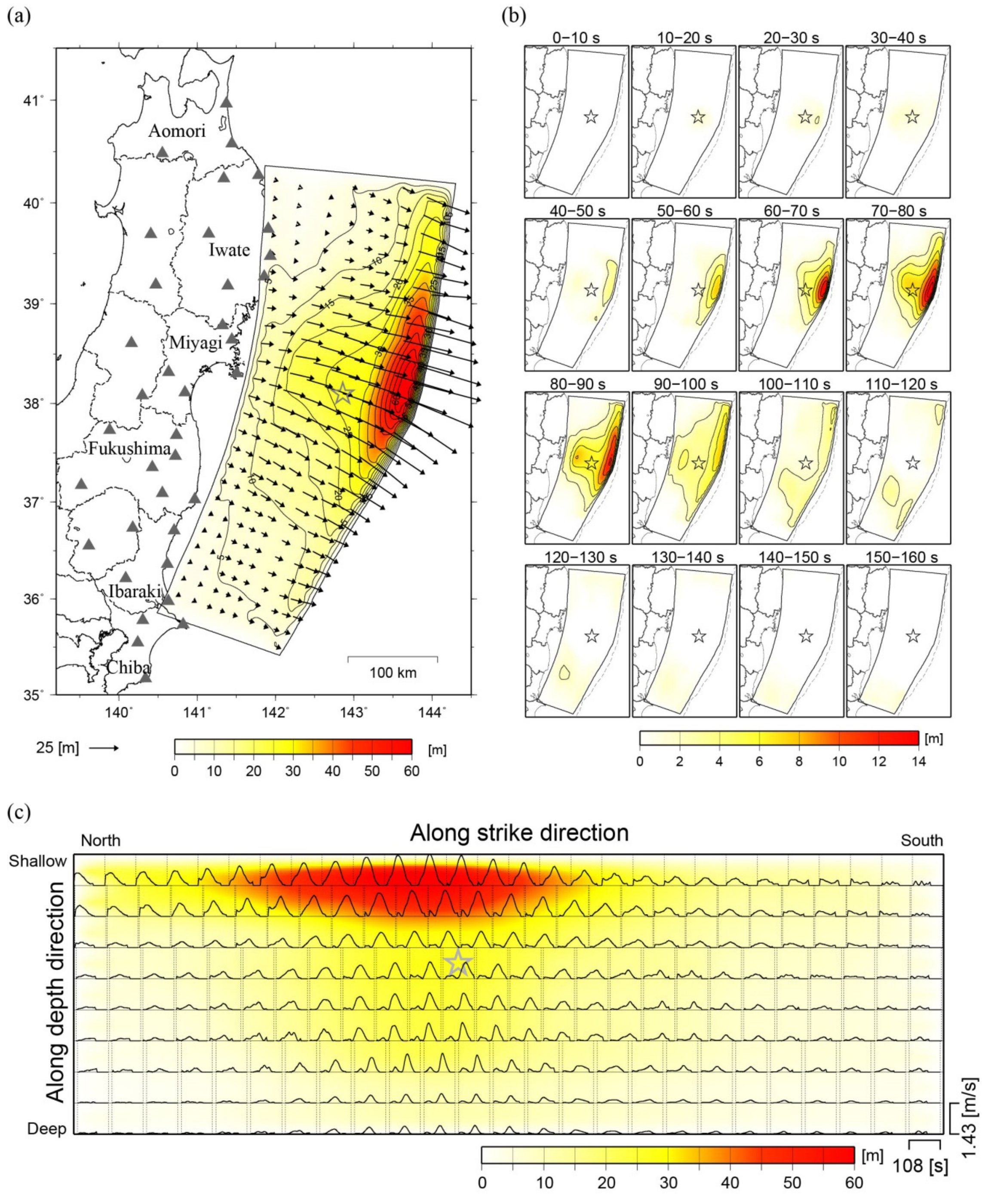

Fig. 4 (a) Total slip distribution and (b) rupture progression process, and (c) slip velocity time functions of each subfault with the total slip distribution in the background, derived for the mainshock. A star denotes the rupture starting point. The contour intervals for the slip distribution and rupture progression process are 5 m and 2 m, respectively. The direction of the arrows in (a) denotes the slip direction of the hanging wall side.

slip model is 5.57×10^{22} Nm (M_W9.1). For the temporal rupture evolution in **Fig. 4b**, the first 40-s rupture, which at first propagated to the shallow part and then reversed to the deeper part, was relatively small. From 40 s after the initial break, the shallower slip started to grow in the Miyagi-Oki region, and was maximum at approximately 80 s. This shallower rupture continued for as long as 70 s, as seen in the slip velocity functions (**Fig. 4c**). Together with this shallow and long rupture event, the rupture expanded to the deeper part from 60 s after the initial break, reaching the deepest edge between 70 s and 80 s. Thus, the two rupture events can be recognized in the Miyagi-Oki region at depths of

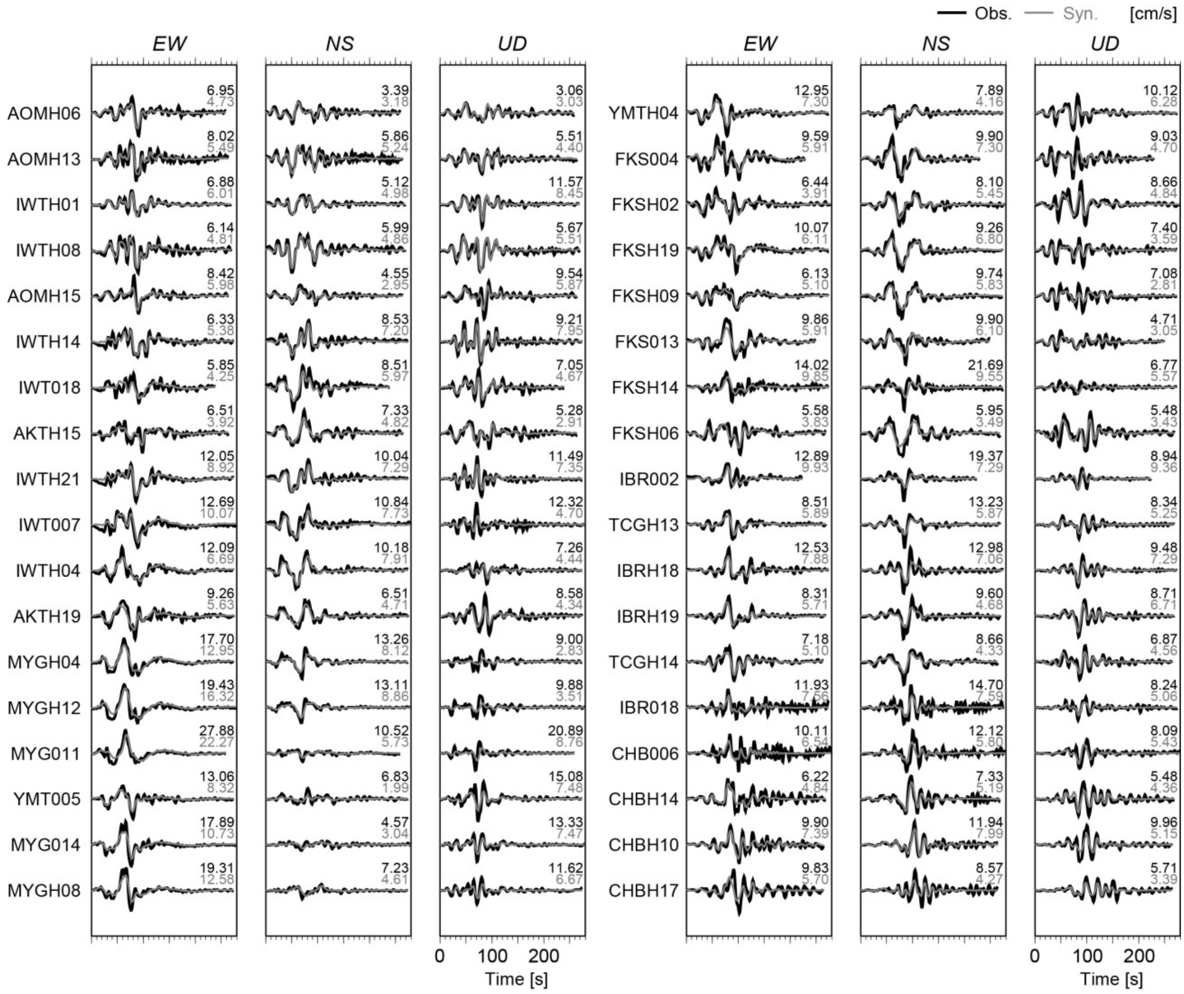

Fig. 5 Comparison between the observed and the synthetic waveforms for the mainshock.

the rupture starting point or deeper. After 100 s, the rupture propagated southward through the Fukushima-Oki and Ibaraki-Oki regions. The panel of the slip velocity function shows that this southern rupture propagation occurred later than the first time window starting times, which were set to be slower than the northern and central parts of the fault. The rupture model reproduced the synthetic waveforms, which fit the observation fairly well from the northern to southern stations (**Fig. 5**).

Overall, the estimated slips were relatively larger than those of the rupture model derived from a rectangular fault model[2),7)]. In addition, the significant rupture of the shallow large slip area started earlier for the curved fault model than for the rectangular fault model. This is probably because the shallow large slip area for the curved fault model was located further from the land, and an earlier slip occurrence was required for the seismic waves from the shallow slip along the Japan Trench to arrive at the same time as that from the closer shallow slip area of the rectangular fault model. Nevertheless, the main characteristics of the rupture pattern were consistent between the two models. One interesting feature of the mainshock rupture found in the two models is that the slip direction of the shallow large slip area appears to radiate out from the largest slip as a center. Namely, the slip directions at the northern and southern subfaults rotated counterclockwise and clockwise, respectively, although the rotation of the northern slip is not so clear in the slip model of this study. This feature has also been found in the slip distribution derived in other studies[4),6)]. An intuitive speculation on the reason of this feature is that the area neighboring the very large slip rotated and formed such a slip pattern. The slip model deduced using the geodetic data including the seafloor observation[6)] had a very large shallow slip in a more concentrated area, which may be better resolved by using the data just above the slip area than this study. A strong contrast in the slip amount may form such a radial pattern in the slip direction.

4. M_{JMA}7.4 Iwate-Oki Aftershock

4.1 Data and Analysis

The velocity waveforms of the three K-NET surface and 15 KiK-net borehole stations along the east coast of the Tohoku district from the Aomori to Miyagi prefectures were used for the inversion analysis of the *M*7.4 Iwate-Oki aftershock in the northern part of the Tohoku-Oki source area (**Fig. 6a**). They were bandpass filtered between 0.01 and 0.167 Hz. The distances from the epicenter to the used stations ranged from 60 km to 200 km. Although the original acceleration records contained several phases from the smaller earthquakes, particularly at the southern stations; these phases disappeared after the bandpass filtering.

The assumed fault model spanned approximately 55 km along the strike and 80 km along the dip (**Figs. 1** and **6a**). The model was divided into subfaults, the horizontal and along-dip intervals of which are 6 km and approximately 6 km, respectively (**Table 1**). A 10.5-s slip after the first time window starting time was allowed for all the subfaults by using the six time windows with 3.0-s durations.

4.2 Result

The inversion results from various *Vr* values show that the faster *Vr* of up to 5 km/s presented the smaller residual value. This situation sometimes occurs in the inversion analysis using multiple time windows[27]. As the slip distributions were similar and the reduction of the residual values became small among the inversions using *Vr* of 3.6 km/s or faster, the result derived using *Vr* of 3.6 km/s was chosen as the preferred rupture model of the Iwate-Oki aftershock. The results are summarized in **Fig. 6**. The slip distribution in **Fig. 6a** shows that a large slip area extended around the hypocenter, particularly to the shallower part of the rupture starting point. A maximum slip of 3.7 m was derived for the southern subfault next to the rupture starting subfault. The seismic moment is 1.54×10^{20} Nm (M_W7.4). **Fig. 6b** shows that the main rupture started 2 s after the initial break to the south of the rupture starting point. The rupture propagated to the shallower part and continued for approximately 10 s, breaking the large slip area found in **Fig. 6a**. It can be seen from **Fig. 6c** that the large slip area had the slip velocity function that initiated with a peak and rapidly decayed as an exponential function. **Fig. 6d** shows the comparison between the observed and synthetic waveforms used in the inversion. The waveform data used here are relatively simple and seem to be less affected by the secondary waves or waves due to other earthquakes. The synthetic waveforms fit the observed ones fairly well.

A few studies[28),29)] have published the source model of the Iwate-Oki aftershock, using the static displacement recorded by GNSS on land. The estimated rectangular fault model with a uniform slip[28)] was located at almost the same location as the large slip area found in this study. In the heterogeneous slip model[29)], the slips were distributed over wider areas, probably because they were derived using much larger subfaults. Nevertheless, the large slip area derived in this study is located within the largest slip contour of the model from the GNSS data[29)] and the two results are considered consistent.

5. M_{JMA}7.6 Ibaraki-Oki Aftershock

5.1 Data and Analysis

For the analysis of the Ibaraki-Oki aftershock, we used the strong-motion data of the 5 K-NET surface stations and 14 KiK-net borehole stations, which were located within 170 km from the epicenter (**Fig. 7a**). The analyzed frequency range was between 0.01 and 0.125 Hz. The high-frequency limit of the frequency range, 0.125 Hz, was lower than that for the Iwate-Oki aftershock analysis, and the same as the Tohoku-Oki mainshock analysis. This limit was selected to avoid the effect of the later secondary-generated phases, which appear in the waveforms of the southern stations located on the deep sedimentary basin. The dimensions of the fault model were approximately 90 km along the strike by 80 km along the dip (**Figs. 1** and **7a**). The subfault size was approximately 10 km × 10 km (**Table 1**). The preliminary examination suggested that a relatively long slip duration is necessary for the area at and around the rupture starting point. Therefore, a 26-s slip was allowed by assigning 12 time windows with 4-s durations to the subfaults. As for the mainshock analysis, the allowed maximum slip durations, i.e., the number of time windows, were reduced for the subfaults located further from the rupture starting point near the fault edges. Then, we set a 22-s slip duration for the second outer subfaults and an 18-s slip duration for the outermost subfaults.

5.2 Result

The result derived using *Vr* of 2.8 km/s was chosen as the preferred rupture model because it gave the smallest residual value among the results with *Vr* ranging from 2.0 to 4.0 km/s. **Fig. 7** shows the derived rupture model of the Ibaraki-Oki aftershock. The derived slip distribution in **Fig. 7a** shows one large slip peak located in the shallower part, to the southeast of the rupture starting point. The large slip area appears as an ellipse with an extended part to the southern direction. The maximum slip was 9.3 m and the seismic moment was 1.04×10^{21} Nm (M_W7.9). The moment magnitudes derived by moment tensor inversion were 7.8 from F-net or 7.9 from the Global CMT project[14)]. The rupture progression shown in **Fig. 7b** indicates that after the small initial 5-s rupture, the rupture propagated to the southeast and became large after 10 s, continuing on the above-mentioned elliptical area until approximately 30 s after the initial break. The

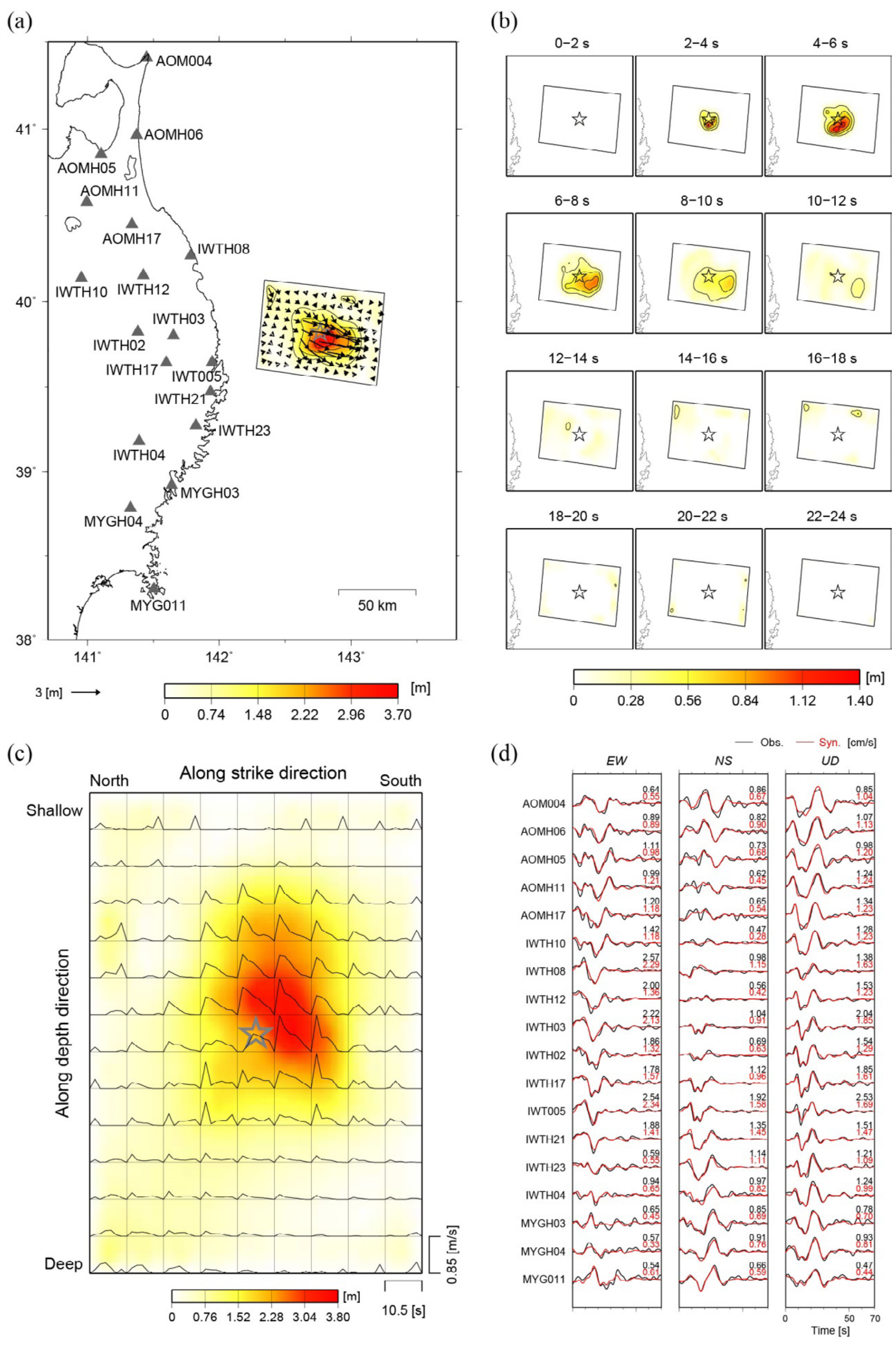

Fig. 6 Inversion result derived for the Iwate-Oki aftershock. (a) Slip distribution together with the strong-motion stations used in the inversion. The contour interval is 0.74 m. (b) Rupture progression in terms of slip amount every 2 s. The contour interval is 0.28 m. (c) Slip velocity time functions of each subfault with the total slip distribution in the background. (d) Comparison between the observed waveforms in black and the synthetic waveforms in red.

slip-velocity functions of the subfaults in this elliptical large slip area reached a peak at the head of the function (**Fig. 7c**), particularly for the subfaults located at the edge of the slip area. **Fig. 7d** shows the comparison between the observed and the synthetic waveforms. The relatively simple observed waveforms were well reproduced by the synthetics.

Some studies derived the source model of the Ibaraki-Oki aftershock from the static displacements observed on land. A rectangular fault model proposed based on the geodetic data[28] well corresponded to the large slip area derived in this

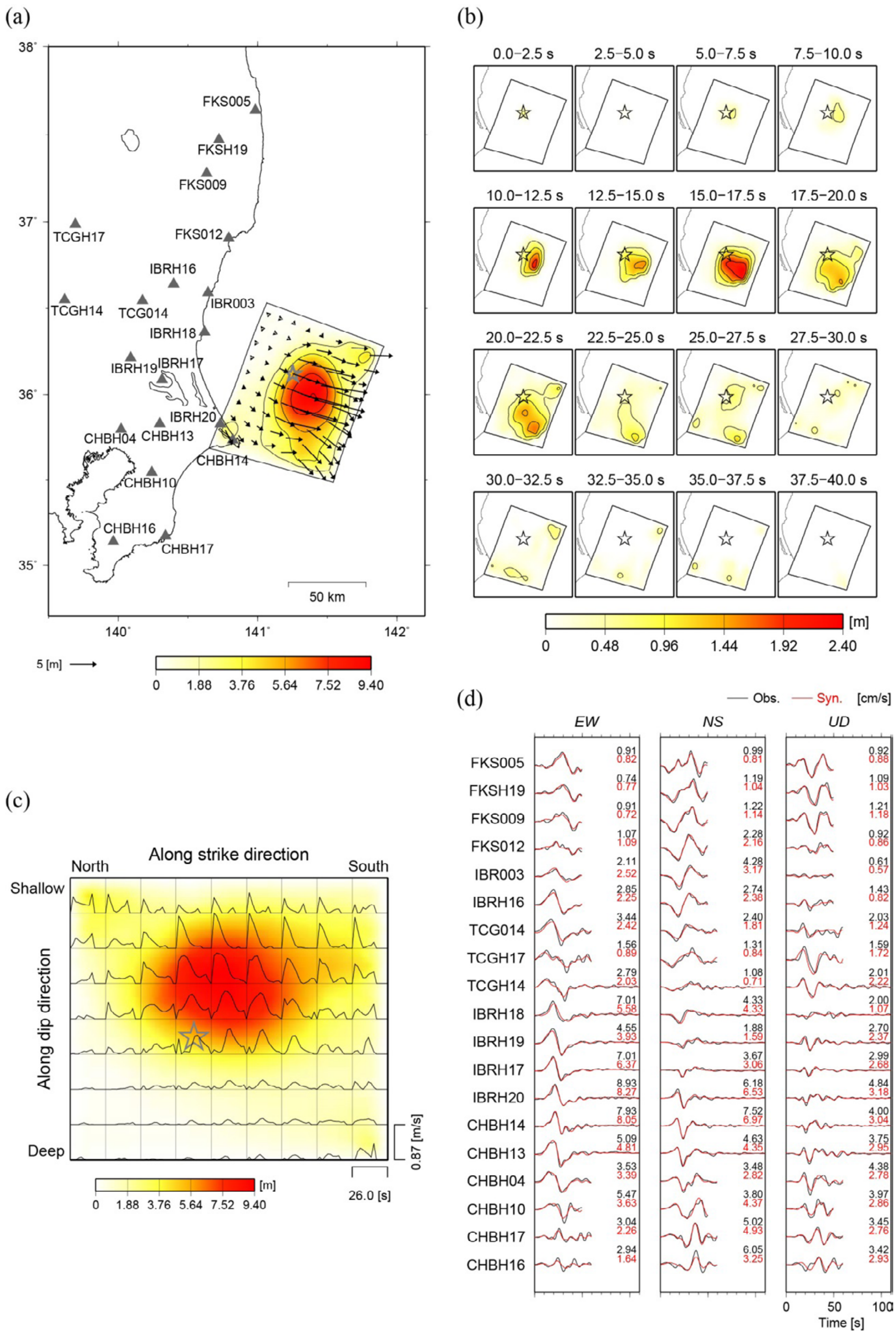

Fig. 7 Inversion result derived for the Ibaraki-Oki aftershock. (a) Slip distribution together with the strong-motion stations used in the inversion. The contour interval is 1.88 m. (b) Rupture progression in terms of slip amount every 2.5 s. The contour interval is 0.48 m. (c) Slip velocity time functions of each subfault with the total slip distribution in the background. (d) Comparison between the observed waveforms in black and the synthetic waveforms in red.

study. Heterogeneous slip models derived from the geodetic data[29),30)] were consistent with the results in this study, although we could not compare them in detail because of the coarse parametrization in these analyses using the geodetic data, as is the case for the Iwate-Oki aftershock. The spatio-temporal slip distribution of the Ibaraki-Oki aftershock was derived from the joint inversion of the strong-motion waveforms and the GNSS static displacements[31)]. The slip model[31)] had a large slip area located to the southeast of the rupture starting point, similar to the result in this study; however, the shape of the large slip area, which did not include the area around the rupture staring point, was somewhat different from that derived in this study. One possible reason for the difference is that the study[31] used a shorter maximum slip duration (16 s) than that of this study (26 s) for the subfaults around the rupture starting point. This may be supported by a more recent study using a new inversion framework and Green's function considering a three-dimensional underground structure model[32]. By allowing a 20-s slip duration, the study[32] derived a large slip area extending from the rupture starting point, as is the case for the result of this study. The spatio-temporal source model was also derived from the back projection of 0.1–1.0 Hz strong-motion waveforms using the dense array in the Kanto district[33]. The result[33] showed that the large energy release occurred to the north of the rupture starting point and propagated landward from 9 to 21 s after the origin time, which is substantially different from the rupture pattern found in our result and other waveform inversion results[31),32]. The difference of the analyzed frequency range may be one of the reasons of this discrepancy, which is the marked nature found for the Tohoku-Oki mainshock[3),8),9], reflecting a depth-dependent variation of the subduction-zone interplate earthquakes[34].

6. Discussions

Fig. 8 compares the slip distributions of the three earthquakes, and the location of the past large earthquakes ($M_{\mathrm{JMA}}\geq 7.0$) from 1922 to the foreshock of the Tohoku-Oki event (11:45, March 9, 2011, $M_{\mathrm{JMA}}7.3$) denoted by the blue circles based on the hypocenter catalog determined by the JMA. Each circle occupies the area equivalent to the rupture area for its magnitude, roughly calculated from the scaling relationship for subduction-zone earthquakes[35]. The spatial distribution of large earthquakes suggested by a figure similar to **Fig. 8** motivated a modeling of the Tohoku-Oki mainshock rupture growth as a result of the multiscale ruptures of existing slip patches[36]. In addition, based on the F-net moment tensor catalog from 1997 to September 2019, we plotted the earthquakes whose source mechanism and depth were consistent with those of the Pacific plate at the location of their epicenter. The maximum differences between the selected thrust earthquakes and the upper surface of the Pacific plate were 20° for the strike and dip angles, and 20 km for the depth. The selected earthquakes should have a rake angle that differed from the pure dip slip angle within 25°. The thrust earthquakes were divided into three groups according to the origin time. The three groups respectively include the earthquakes that occurred from 1997 until just before the foreshock of the Tohoku-Oki event, those from the foreshock until just before the mainshock, and those after the Ibaraki-Oki aftershock.

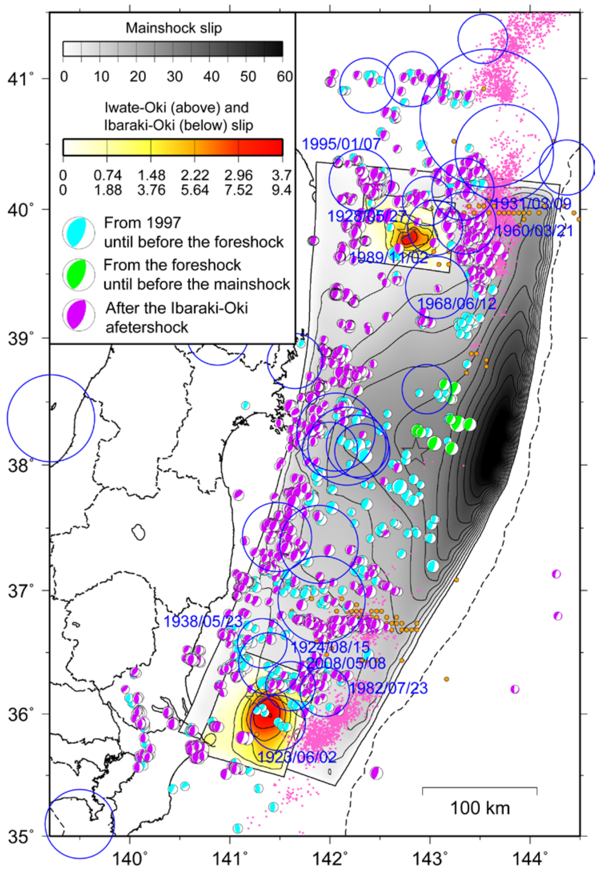

Fig. 8 Comparison of the slip distribution of the three analyzed earthquakes together with the large earthquakes ($M_{\mathrm{JMA}}\geq 7.0$) that occurred since 1922 until just before the Tohoku-Oki foreshock (blue circles), the earthquakes that have source mechanisms and depths are consistent with the Pacific plate from 1997 to September 2019, and two types of slow earthquakes (orange dots: very-low-frequency earthquakes from January 2014 to August 2018, pink dots: tectonic tremors from August 2016 to August 2018)[41]. The blue circles have areas equivalent to the rupture area in terms of magnitude. The beachballs are colored according to the period of the earthquake occurrence.

The large slip areas of the two aftershocks are located close to but outside the 5-m contour line of the mainshock slip. The slip areas of the mainshock and the two aftershocks are complementary, given that a slip of 5 m for the mainshock is relatively small considering uncertainties of slips and a possibility of wider estimated slip areas than the actual ones due to the smoothing constraint. Many pre-foreshock thrust earthquakes (light blue beachballs in **Fig. 8**) occurred in the Miyagi-Oki and Fukushima-Oki regions in which a ~25-m slip was estimated for the mainshock, although there were no such earthquakes in the shallower larger slip area. The foreshock sequence (green beachballs), which has been considered precursory activity of the mainshock[37),38)], is found in the area where the pre-foreshock activity was low and the larger slip was estimated for the mainshock. The thrust aftershocks (purple beachballs) tend to have occurred near the 10-m mainshock slip contours, in the northern and southern source areas at the mainshock hypocentral depth (~15 km), and in the deeper edges of the mainshock fault. The seismicity of the thrust aftershocks is notable around the slip areas of the two *M*7 aftershocks, but few are found just within the slip areas. These observations suggest that the complimentary nature prevails in smaller interplate earthquakes as well as among the mainshock and the two large aftershocks.

From the lessons of the Tohoku-Oki earthquake and tsunami disasters, the dense seafloor observation network named S-net comprised seismometers and pressure gauges was constructed and operated in the Pacific Ocean along the Japan Trench by NIED[39)]. Taking advantage of the seafloor observation, tectonic tremor activities along the Japan Trench, which had not been directly observed before, have recently been detected using S-net data[40),41)]. To examine the relationship between the rupture models derived in this study and slow earthquakes, the location of these tectonic tremors detected for two years since August 2016 and the very-low-frequency earthquakes from January 2014 to August 2018 [40),41),42)] are also plotted in **Fig. 8**. The tectonic tremors occurred in both the Iwate-Oki and Ibaraki-Oki regions at 10–20 km depth contours of the Pacific plate interface. The slip areas of the two *M*7-class aftershocks were located at deeper regions than the tectonic tremors. For the Ibaraki-Oki aftershock, the top of the large slip area even seems to be delimited by the tremor activity area. The very-low-frequency earthquakes are located outside of the slip areas of the two aftershocks. As a result, the complementarity between the large slip areas and slow earthquakes, which has already been found for the mainshock and the past earthquakes[41)], was also found for the two *M*7-class aftershocks.

Fig. 8 shows that near the slip area of the Iwate-Oki aftershock, M_{JMA} 7.2 and 7.1 earthquakes occurred in 1960 and 1989, respectively. The rupture processes of these previous earthquakes, which have a source mechanism consistent with interplate earthquakes, were estimated from waveform inversion[43)]. **Fig. 9a** compares the slip distributions of these earthquakes[43)] and the 2011 Iwate-Oki aftershock. While the hypocenters were located to the east of the 2011 event, the large slip areas of the previous earthquakes almost overlap the large slip area of the 2011 Iwate-Oki aftershock. Meanwhile, the magnitude and slip amplitude of the 2011 event were a little larger than those of the previous ones, as M_W of the 1960 and 1989 events were 7.0 and 7.0–7.3, respectively[43)]. A time interval from the previous earthquake was slightly shorter for the 2011 aftershock than for the 1989 earthquake. The 2011 Iwate-Oki aftershock may have occurred and been hastened as a consequence of the stimulation of the area where earthquakes with similar size have occurred by the Tohoku-Oki earthquake.

A few *M*7-class earthquakes are plotted in and around the slip area of the Ibaraki-Oki aftershock in **Fig. 8**. The circle denoting the 1923 event overlaps the slip area of the 2011 event; however, the 1923 event is too old for further examination of the relationship with the 2011 event. **Fig. 9b** shows the comparison among the slip distributions of the 1982 event[44)], 2008 event[45)], and 2011 event. The slip areas of the two previous earthquakes slightly overlap the large slip area of the 2011 aftershock but do not correspond to its peak slip area. The magnitude of the 2011 event was much larger than those of the other two events. For the Ibaraki-Oki aftershock, the Tohoku-Oki mainshock may have triggered the earthquake in neighboring areas that had been preparing to rupture in a different pattern from that found in the Iwate-Oki region.

To highlight the rupture characteristics of the two *M*7-class aftershocks, we compared them with the previous significant interplate earthquake with similar magnitude in the other regions in Japan analyzed using the strong-motion data. The 1978 Miyagi-Oki earthquake occurred between the subducting Pacific plate and overriding plate with M_W of 7.4, which is the same situation as the Iwate-Oki aftershock. The rupture process of this interplate earthquake was well

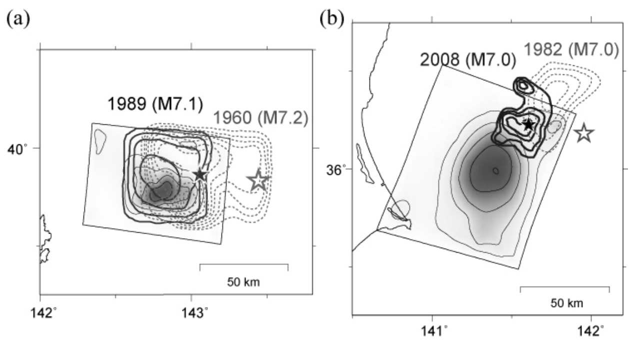

Fig. 9 Comparison of the slip distributions between the 2011 Tohoku-Oki aftershocks (thin contour line with gray color contour) and the past significant earthquakes read from the previous source inversion studies[43),44),45)]. Stars denote the rupture starting point of the past earthquakes (a) Iwate-Oki aftershock compared with the 1960 event[43)] (dotted contours with a gray star) and the 1989 event[43)] (solid contours with a black star). (b) Ibaraki-Oki earthquake compared with the 1982 event[44)] (dotted contours with a gray star) and 2008 event[45)] (solid contours with a black star).

examined using the strong-motion records[26]. While the slip model of the Iwate-Oki aftershock can be characterized by one slip patch, the 1978 Miyagi-Oki earthquake has one major slip area together with some moderate slips areas that were not negligible, as the moderate slip areas corresponded to slip areas of the repeated M_W7.2 event in 2005 [26]. The slip model of the Iwate-Oki aftershock was simpler and more compact than the 1978 Miyagi-Oki earthquake. The rupture progression of the Iwate-Oki aftershock was also simpler and ceased in a shorter duration.

For the Ibaraki-Oki aftershock, one comparable interplate event in Japan is the 1923 Kanto earthquake, which occurred between the subducting Philippine Sea plate and the overriding plate in the southern Kanto region, to the south of the Tokyo metropolitan area. Although it is an old event, the spatio-temporal rupture process was examined[46], in which the moment magnitude was estimated to be 8.0 (1.1×10^{21} Nm) from the joint inversion of the geodetic, teleseismic, and strong-motion data. The slip distribution[46] indicated that the Kanto earthquake had two large slip peaks, which were approximately 60 km apart. It took approximately 40 s to rupture the two slip areas. As seen in **Fig. 7**, the Ibaraki-Oki aftershock had one large slip area that ruptured within 25 s. Its rupture process is, then, considered simpler than the 1923 Kanto earthquake.

We take another example for the comparison with the Ibaraki-Oki aftershock. The 1994 Sanriku-Haruka-Oki earthquake was an M_W7.7 interplate event that occurred to the north of the Tohoku-Oki mainshock source area between the Pacific and continental plates. An inversion analysis using strong-motion data[47] showed a complex rupture process of the Sanriku-Haruka-Oki earthquake, in which the rupture evolved through some stages propagating along more than 120 km and continued for nearly 60 s, despite its smaller magnitude than the Ibaraki-Oki aftershock. The comparisons above suggest that the rupture of the two large aftershocks of the Tohoku-Oki earthquakes tend to be simple regarding their magnitudes.

7. Conclusions

The rupture processes of the Tohoku-Oki mainshock and the two *M*7-class aftershocks were deduced from the strong-motion data considering the Pacific plate geometry. Although the main characteristics of the mainshock rupture derived from the rectangular fault were found for the curved fault result, the use of the curved fault enabled further examination of the Tohoku-Oki earthquake, such as the waveform simulation and/or source inversion using a three-dimensional underground structure model. We found similar and different characteristics between the two large aftershocks. The former is their simple spatio-temporal rupture process compared with interplate earthquakes of similar magnitude. The latter is the relationship of the rupture area with those of the previous earthquakes in the region. The Iwate-Oki aftershock ruptured the same area as previous earthquakes with similar magnitudes whereas the Ibaraki-Oki aftershock was the largest earthquakes rupturing the area where no significant earthquakes occurred in the past approximately 90 years. For the Ibaraki-Oki aftershock, the derived rupture process was evidently different from the source model from the higher-frequency strong motions, suggesting the possibility of the different wave radiation depending on the frequency band, which is an interesting topic for further study. In addition, recent studies using the new seafloor observation networks revealed a notable feature between the large earthquakes and slow earthquakes, which would provide a new scope of research on subduction-zone earthquakes.

Acknowledgements

We used the hypocenter catalog determined by the JMA. This study was partially supported by French–Japanese ANR-JST project DYNTOHOKU (2011–2013).

References

1) Lay, T. (2018): A review of the rupture characteristics of the 2011 Tohoku-oki Mw 9.1 earthquake. Tectonophysics, **733**, 4-36, doi:10.1016/j.tecto.2017.09.022.
2) Suzuki, W., Aoi, S., Sekiguchi, H., and Kunugi, T. (2011): Rupture process of the 2011 Tohoku-Oki mega-thrust earthquake (M9.0) inverted from strong-motion data. Geophys. Res. Lett., **38**, L00G16, doi:10.1029/2011GL049136.
3) Ide, S., Baltay, A., and Beroza, G. C. (2011): Shallow dynamic overshoot and energetic deep rupture in the 2011 M_W 9.0 Tohoku-Oki earthquake. Science, **332**, 1426-1429, doi:10.1126/science.1207020.
4) Yue, H. and Lay, T. (2011): Inversion of high-rate (1 sps) GPS data for rupture process of the 11 March 2011 Tohoku earthquake (M_W 9.1). Geophys. Res. Lett., **38**, L00G09, doi:10.1029/2011GL048700.
5) Saito, T., Ito, Y., Inazu, D., and Hino, R. (2011): Tsunami source of the 2011 Tohoku-Oki earthquake, Japan: Inversion analysis based on dispersive tsunami simulations. Geophys. Res. Lett., **38**, L00G19, doi:10.1029/2011GL049089.
6) Iinuma, T., Hino, R., Kido, M., Inazu, D., Osada, Y., Ito, Y., Ohzono, M., Tsushima, H., Suzuki, S., Fujimoto, H., and Miura, S. (2012): Coseismic slip distribution of the 2011 off the Pacific Coast of Tohoku Earthquake (M9.0) refined by means of seafloor geodetic data. J. Geophys. Res., **117**, B07409, doi:10.1029/2012JB009186.

7) Suzuki, W., Aoi, S., Sekiguchi, H., and Kunugi, T. (2012): Source rupture process of the 2011 off the Pacific Coast of Tohoku Earthquake derived from strong-motion records. Natural Disaster Research Report, **48**, National Research Institute for Earth Science and Disaster Prevention, 53-62 (in Japanese).
8) Koper, K. D., Hutko, A. R., Lay, T., Ammon, C. J., and Kanamori, H. (2011): Frequency-dependent rupture process of the 2011 M_W 9.0 Tohoku Earthquake: Comparison of short-period P wave backprojection images and broadband seismic rupture models. Earth Planets Space, **63**, 599-602, doi:10.5047/eps.2011.05.026.
9) Kurahashi, S. and Irikura, K. (2011): Source model for generating strong motions during the 2011 off the Pacific coast of Tohoku Earthquake. Earth Planets Space, **63**, 571-576, doi:10.5047/eps.2011.06.044.
10) Fukuyama, E., Ishida, M, Dreger, D. S., and Kawai, H. (1998): Automated seismic moment tensor determination by using on-line broadband seismic waveforms. J. Seismol. Soc. Japan (Zisin) II, **51**, 149-156, doi:10.4294/zisin1948.51.1_149 (in Japanese).
11) Yasuda, S., Harada, K., Ishikawa, K., and Kanemaru, Y. (2012): Characteristics of liquefaction in Tokyo Bay area by the 2011 Great East Japan Earthquake. Soils and Foundations, **52**, 792-810, doi:10.1016/j.sandf.2012.11.004.
12) National Research Institute for Earth Science and Disaster Resilience (2019): NIED K-NET, KiK-net, National Research Institute for Earth Science and Disaster Resilience, doi:10.17598/NIED.0004.
13) Aoi, S., Kunugi, T., Nakamura, H. and Fujiwara, H. (2011): Deployment of new strong motion seismographs of K-NET and KiK-net, in “Earthquake Data in Engineering Seismology” ed. by S. Akkar, P. Gülkan, and T. van Eck, Geotechnical, Geological, and Earthquake Engineering, **14**, Springer, Dordrecht, 167-186, doi:10.1007/978-94-007-0152-6_12.
14) Nettles, M., Ekström, G., and Koss, H. C. (2011): Centroid-moment-tensor analysis of the 2011 off the Pacific coast of Tohoku Earthquake and its larger foreshocks and aftershocks. Earth Planets Space, **63**, 519-523, doi:10.5047/eps.2011.06.009.
15) Koketsu, K., Miyake, M., and Suzuki, H. (2012): Japan integrated velocity structure model version 1. In “Proceedings of the 15th World Conference on Earthquake Engineering”, Lisbon, 10463-10466.
16) Koketsu, K., Miyake, H., Afnimar, and Tanaka, Y. (2009): A proposal for a standard procedure of modeling 3-D velocity structures and its application to the Tokyo metropolitan area, Japan. Tectonophysics, **472**, 290-300, doi:10.1016/j.tecto.2008.05.037.
17) Piegl, L. and Tiller, W. (1997): The NURBS Book, 2nd Ed., Springer, 646 pp.
18) Olson, A. H. and Apsel, R. J. (1982): Finite faults inverse theory with application to the 1979 Imperial Valley earthquake. Bull. Seismol. Soc. Am., **72**, 1969-2001.
19) Hartzell, S. H. and Heaton, T. H. (1983): Inversion of strong ground motion and teleseismic waveform data for the fault rupture history of the 1979 Imperial Valley, California, earthquake. Bull. Seismol. Soc. Am., **73**, 1553-1583.
20) Wald, D. J., Helmberger, D. V., and Heaton, T. H. (1991): Rupture model of the 1989 Loma Prieta earthquake from the inversion of strong-motion and broadband teleseismic data. Bull. Seismol. Soc. Am., **81**, 5, 1540-1572.
21) Bouchon, M. (1981): A simple method to calculate Green’s function for elastic layered media. Bull. Seismol. Soc. Am., **71**, 959-971.
22) Kennett, B. L. N. and Kerry, N. J. (1979): Seismic waves in a stratified half space. Geophys. J. R. Astron. Soc., **57**, 557-583, doi:10.1111/j.1365-246X.1979.tb06779.x.
23) Lawson, C. L. and Hanson, R. J. (1974): Solving Least Squares Problems. Prentice-Hall, Inc., New Jersey, 340 pp.
24) Sekiguchi, H., Irikura, K., and Iwata, T. (2000): Fault geometry at the rupture termination of the 1995 Hyogo-ken Nanbu earthquake. Bull. Seismol. Soc. Am., **90**, 117-133, doi:10.1785/0119990027.
25) Yoshida, S. (1989): Waveform inversion using ABIC for the rupture process of the 1983 Hindu Kush earthquake. Phys. Earth Planet. Inter. **56**, 389–405, doi:10.1016/0031-9201(89)90172-6.
26) Wu, C., Koketsu, K., and Miyake, H. (2008): Source processes of the 1978 and 2005 Miyagi-oki, Japan, earthquakes: Repeated rupture of asperities over successive large earthquakes. J. Geophys. Res., **113**, B08316, doi:10.1029/2007JB005189.
27) Hartzell, S., Mendoza, C., and Zeng, Y. (2013): Rupture model of the 2011 Mineral, Virginia, earthquake from teleseismic and regional waveforms. Geophys. Res. Lett., **40**, doi:10.1002/2013GL057880.
28) Nishimura, T., Munekane, H., and Yarai, H. (2011): The 2011 off the Pacific coast of Tohoku Earthquake and its aftershocks observed by GEONET. Earth Planets Space, **63**, 631-636, doi:10.5047/eps.2011.06.025.
29) Miyazaki, S., McGuire, J. J., and Segall, P. (2011): Seismic and aseismic fault slip before and during the 2011 off the Pacific coast of Tohoku Earthquake. Earth Planets Space, **63**, 637-642, doi:10.5047/eps.2011.07.001.
30) Ito, T., Ozawa, K., Watanabe, T., and Sagiya, T. (2011): Slip distribution of the 2011 of the Pacific coast of Tohoku

Earthquake inferred from geodetic data. Earth Planets Space, **63**, 627-630, doi:10.5047/eps.2011.06.023.

31) Kubo, H., Asano, K., and Iwata, T. (2013): Source-rupture process of the 2011 Ibaraki-oki, Japan, earthquake (M_W 7.9) estimated from the joint inversion of strong-motion and GPS data: Relationship with seamount and Philippine Sea Plate. Geophys. Res. Lett., **40**, 3003-3007, doi:10.1002/grl.50558.
32) Kubo, H., Asano, K., Iwata, T., and Aoi, S. (2016): Development of fully Bayesian multiple-time-window source inversion. Geophys. J. Int., **204**, 1601-1619, doi:10.1093/gji/ggv540.
33) Honda, R., Yukutake, Y., Ito, H., Harada, M., Aketagawa, T., Yoshida, A., Sakai, S., Nakagawa, S., Hirata, N., Obara, K., Matsubara, M., and Kimura, H. (2013): Rupture process of the largest aftershock of the *M* 9 Tohoku-oki earthquake obtained from a back-projection approach using the MeSO-net data. Earth Planets Space, **65**, 917-921, doi:10.5047/eps.2013.01.003.
34) Lay, T., Kanamori, H., Ammon, C. J., Koper, K. D., Hutko, A. R., Ye, L., Yue, H., Rushing, T. M. (2012): Depth-varying rupture properties of subduction zone megathrust faults. J. Geophys. Res., **117**, B04311, doi:10.1029/2011JB009133.
35) Murotani, S., Satake, K., and Fujii, Y. (2013): Scaling relations of seismic moment, rupture area, average slip, and asperity size for *M*~9 subduction-zone earthquake. Geophys. Res. Lett., **40**, 5070-5074, doi:10.1002/grl.50976.
36) Ide, S. and Aochi, H. (2013): Historical seismicity and dynamic rupture process of the 2011 Tohoku-Oki earthquake, Tectonophysics, **600**, 1-13, doi:10.1016/j.tecto.2012.10.018.
37) Ando, R. and Imanishi, K. (2011): Possibility of M_W 9.0 mainshock triggered by diffusional propagation of after-slip from M_W 7.3 foreshock. Earth Planets Space, **63**, 767-771, doi:10.5047/eps.2011.05.016.
38) Kato, A., Obara, K., Igarashi, T., Tsuruoka, H., Nakagawa, S., and Hirata, N. (2012): Propagation of slow slip leading up to the 2011 M_W 9.0 Tohoku-Oki earthquake. Science, **335**, 705-708, doi:10.1126/science.1215141.
39) Kanazawa, T., Uehira, K., Mochizuki, M., Shinbo, T., Fujimoto, H., Noguchi, S., Kunugi, T., Shiomi, K., Aoi, S., Matsumoto, T., Sekiguchi, S., and Okada, Y. (2016): S-net project, cabled observation network for earthquakes and tsunamis, SubOptic 2016, WE2B–3.
40) Tanaka, S., Matsuzawa, T., and Asano, Y. (2019): Shallow low-frequency tremor in the northern Japan Trench subduction zone. Geophys. Res. Lett., **46**, 5217-5224, doi:10.1029/2019GL082817.
41) Nishikawa, T., Matsuzawa, T., Ohta, K., Uchida, N., Nishimura, T., and Ide, S. (2019): The slow earthquake spectrum in the Japan Trench illuminated by the S-net seafloor observatories. Science, **365**, 808-813, doi:10.1126/science.aax5618.
42) Matsuzawa, T., Asano, Y., and Obara, K. (2015): Very low frequency earthquakes off the Pacific coast of Tohoku, Japan. Geophys. Res. Lett., **42**, 4318-4325, doi:10.1002/2015GL063959.
43) Yamanaka, Y. and Kikuchi, M. (2004): Asperity map along the subduction zone in northeastern Japan inferred from regional seismic data. J. Geophys. Res., **109**, B07307, doi:10.1029/2003JB002683.
44) Mochizuki, K., Yamada, T., Shinohara, M., Yamanaka, Y., and Kanazawa, T. (2008): Weak interplate coupling by seamounts and repeating *M*~7 earthquakes. Science, **321**, 1194-1197, doi:10.1126/science.1160250.
45) Yamanaka, Y. (2008): NGY Seismological Note, No.7, http://www.seis.nagoya-u.ac.jp/sanchu/Seismo_Note/2008/NGY7.html (in Japanese).
46) Kobayashi, R. and Koketsu, K. (2005): Source process of the 1923 Kanto earthquake inferred from historical geodetic, teleseismic, and strong motion data. Earth Planets Space, **57**, 261-270, doi:10.1186/BF03352562.
47) Nakayama, W. and Takeo, M. (1997): Slip history of the 1994 Sanriku-Haruka-Oki, Japan, earthquake deduced from strong-motion data. Bull. Seismol. Soc. Am., **87**, 918-931.

(Received : November 18, 2019)
(Accepted : December 19, 2019)

曲面断層モデルを用いた 2011 年東北地方太平洋沖地震および 2 つの M7 級余震の震源破壊過程の推定

鈴木　亘[*]・青井　真[*]・関口春子[**]・功刀　卓[*]

[*]防災科学技術研究所　地震津波火山ネットワークセンター
[**]京都大学防災研究所　社会防災研究部門

要　旨

2011 年東北地方太平洋沖地震（M_{JMA}9.0）に引き続いて震源域の北端および南端において M_{JMA}7.4 と M_{JMA}7.6 の 2 つの大きな余震が発生した．本研究では本震および 2 つの *M*7 級余震について断層面を適切に表現するため曲面断層モデルを構築し，防災科学技術研究所の強震観測網 K-NET および KiK-net の強震波形記録を用いて震源破壊過程を推定した．本震については，浅い領域での長時間に及ぶ非常に大きなすべり，深い領域での繰り返しの破壊，南部への遅い破壊伝播など複雑な破壊過程が見られた．一方，2 つの余震の震源破壊過程は時空間的に比較的単純な結果が得られた．推定された 3 地震のすべり分布，逆断層型地震の発生位置および微動・超低周波地震の発生位置は相補的であった．過去 90 年程度の地震と比較すると，岩手県沖の余震は数十年ごとに繰り返している地震の 1 つと考えられるが，茨城県沖の余震はこの領域で最も規模の大きい地震であった．

キーワード：震源破壊過程，東北地方太平洋沖地震，岩手県沖の地震，茨城県沖の地震，曲面断層，強震動